LETTER TO THE EDITOR

Constraining the cosmic-ray ionization rate and their spectrum with NIR spectroscopy of dense clouds

A test-bed for JWST

Shmuel Bialy[1], Sirio Belli[2], and Marco Padovani[3]

[1] Department of Astronomy, University of Maryland, College Park, MD 20742, USA
e-mail: `sbialy@umd.edu`
[2] Harvard Smithsonian Center for Astrophysics, 60 Garden st., Cambridge, MA 02138, USA
[3] INAF-Osservatorio Astrofisico di Arcetri - Largo E. Fermi, 5 - 50125 Firenze, Italy

ABSTRACT

Context. Low-energy cosmic-rays (CRs) control the thermo-chemical state and the coupling between gas and magnetic fields in dense molecular clouds, the sites of star-formation. However, current estimates of the low-energy CR spectrum ($E \lesssim 1$ GeV) and the associated CR ionization rate are highly uncertain.
Aims. We apply, for the first time, a new method for constraining the CR ionization rate and the CR spectral shape using H_2 rovibrational lines from cold molecular clouds.
Methods. Using the MMIRS instrument on the MMT, we obtained deep near-infrared (NIR) spectra in six positions within four dense cores, G150, G157, G163, G198, with column densities $N_{H_2} \approx 10^{22}$ cm^{-2}.
Results. We derive 3σ upper limits on the H_2 $(1-0)$S(0) line (2.22 μm) brightness in the range $I = 5.9 \times 10^{-8}$ to 1.2×10^{-7} erg cm^{-2} s^{-1} sr^{-1} for the different targets. Using both an analytic model and a numerical model of CR propagation, we convert these into upper limits on the CR ionization rate in the clouds' interior, $\zeta = 1.5$ to 3.6×10^{-16} s^{-1}, and lower limits on the low-energy spectral slope of interstellar CR protons, $\alpha = -0.97$ to -0.79. We show that while MMT was unable to detect the H_2 lines due to high atmospheric noise, JWST/NIRSpec will be able to efficiently detect the CR-excited H_2 lines, making it the ideal method for constraining the otherwise elusive low-energy CRs, shedding light on the sources and propagation modes of CRs.

Key words. cosmic rays – ISM: clouds –ISM: lines and bands – Astrochemistry – Infrared: ISM

1. Introduction

Low-energy CRs ($E \lesssim 1$ GeV) play an important role in determining the thermochemical and dynamical state of dense molecular clouds and are thus crucially important for star-formation (see Padovani et al. 2020 for a recent review). These CRs penetrate into large cloud depths and provide the main ionization source in the gas. This ionization is critical: [1] it is the dominant heating mechanism in the gas (Glassgold et al. 2012; Girichidis et al. 2020) [2] it introduces coupling of the gas with magnetic fields (Padovani et al. 2014; Zhao et al. 2020), and [3] it drives the chemistry resulting in the formation of a rich array of interstellar molecules (Dalgarno 2006; Caselli et al. 2012; Indriolo & Mc Call 2013).

Despite their importance, the spectrum of low-energy CRs, and the CR ionization rate, hereafter ζ, remain uncertain[1]. This is because at these energies, direct measurements from Earth and Space are affected by solar modulations (Gloeckler & Fisk 2015; Padovani et al. 2018, see §3.2 for an elaborate discussion). In the interstellar medium, ζ has been estimated using spectroscopic observations that measure the abundances of various trace molecules, H_3^+, OH$^+$, H_2O^+, ArH$^+$, etc., in combination with detailed chemical models. These methods yield a range of ioniza-

tion rates, $\zeta \approx 10^{-17} - 10^{-15}$ s^{-1} in dense and diffuse Galactic clouds (Guelin et al. 1982; van der Tak & van Dishoeck 2000; Indriolo & McCall 2012; Neufeld & Wolfire 2017; Bialy et al. 2019; Gaches et al. 2019) and as high as $\zeta \approx 10^{-14} - 10^{-12}$ s^{-1} towards Galactic center (Le Petit et al. 2016), protostellar cluster (Fontani et al. 2017; Favre et al. 2018) and extragalactic sources (Müller et al. 2015; González-Alfonso et al. 2018). As these ζ values are based on observations of rare molecules, they rely on chemical models which in turn introduces uncertainties (especially in dense clouds), due to uncertainties in the chemical rate coefficients, the limited completeness of the chemical network, and an assumption on the gas volume density.

Recently, Bialy (2020a, hereafter B20) has proposed a new method for deriving ζ in cold molecular clouds that relies on H_2, the main constituent of the gas. The idea is that in dense clouds ($N_{H_2} \sim 10^{22}$ cm^{-2}) H_2 is cold and resides primarily in its ground electronic and rovibrational state. Secondary electrons produced by the penetrating CRs excite the rovibrational states of H_2, which decay to the ground state through photon emission in the NIR. As discussed in B20, for the temperatures and densities typical of these clouds ($T \lesssim 30$ K, $n \sim 10^4 - 10^6$ cm^{-3}), collisional de-excitation is negligible, and thus the flux in the emitted lines is proportional to the CR-H_2 excitation rate and also to ζ. Thus, H_2 rovibrational emission lines may be used to reliably constrain the ionization rate, without the need of chem-

---

[1] In this paper, ζ denotes the total (primary+secondary) ionization rate, per H_2 molecule.
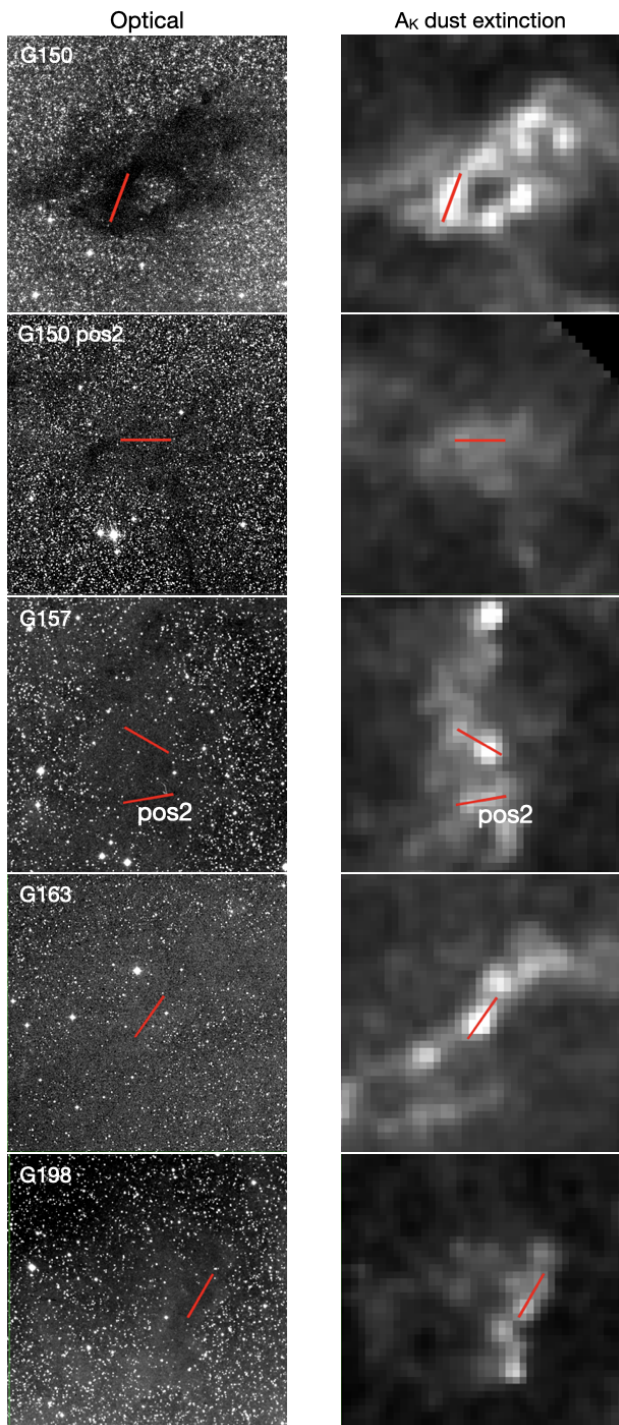
Fig. 1. Optical image and NIR dust attenuation map for our target clouds. Images are from ESA-Sky (Baines et al. 2017), based on DSS and 2MASS (Skrutskie et al. 2006). Each panel is $40' \times 40'$. The position of the $7'$ slit is shown in red.

Fig. 2. Row 1: The 1D spectrum for G150 (see Appendix A for the rest of the targets). The black line is a linear fit to I_λ in the region with no skylines (blue strip). The vertical orange strip is the wavelength of the $(1-0)S(0)$ line. Row 2: $I_{\text{sub,int}}$, the spectrum after we subtracted from it the linear fit and integrated over the instrument spectral resolution, $\Delta\lambda \approx 7.4 \times 10^{-4}\mu$m. Row 3: The error (noise) on $I_{\text{sub,int}}$. Row 4: the SNR $= I_{\text{sub,int}}/\sigma$. Wavelengths are in vacuum.

ical models, or additional assumptions on the gas density and compositions. B20 emphasized the importance of four particular lines: $(1-0)O(2)$, $(1-0)Q(2)$, $(1-0)S(0)$, and $(1-0)O(4)$ at $\lambda = 2.63, 2.41, 2.22, 3.00\,\mu$m respectively (see their Table 1), for which CR excitation dominates over competing excitation processes.

In this paper we report on deep ground-based spectroscopic NIR observations of four nearby dense clouds (§2). We use these observations to derive constraints on ζ, and on the interstellar
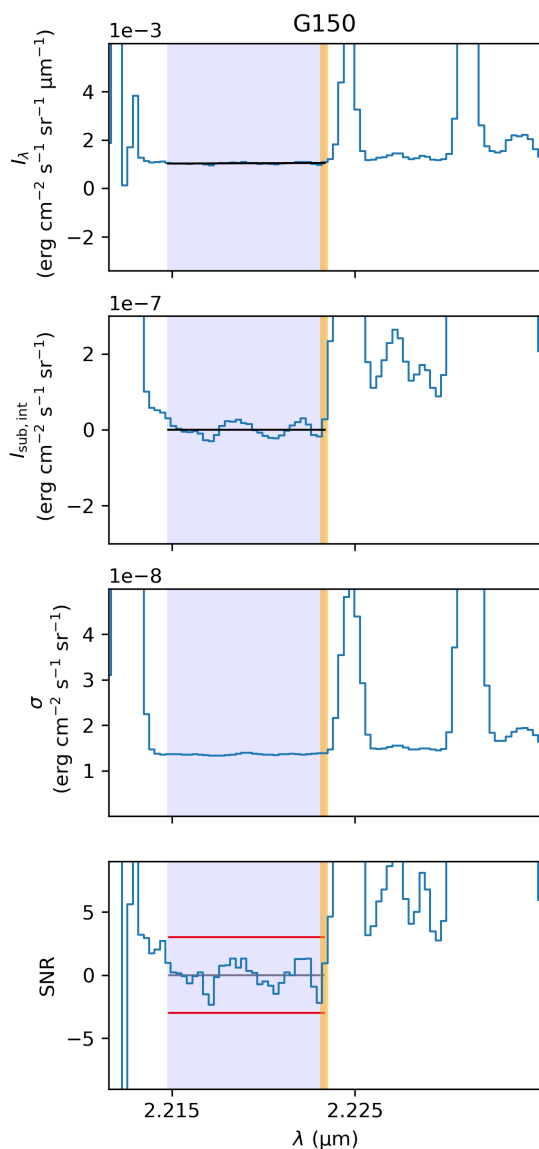
CR proton spectrum at low energies that is impinging on the molecular clouds (§3). This is the first time H$_2$ line emission is used to constrain CR properties. We discuss future prospects for JWST and demonstrate how it will be able to constrain ζ and the interstellar low-energy CR spectrum and its fluctuations (§4).

2. Observations

2.1. The sample

We observed four nearby dense molecular clouds: G150.47+3.93, G157.08-8.69, G163.82-8.44, and G198.58-9.10 (the naming convention is from the Galactic Cold Core, survey; GCC, Juvela et al. 2012). Hereafter we use abbreviated names: G150, G157, G163, and G198. The clouds were selected from the GCC survey based on the following criteria:

1. The cloud should not host, nor be close to, bright stars so that the UV radiation field is weak and the excitation component due to CRs is easier to detect;

2. The cloud is optically thick in the K band, i.e., $N_{H_2} \gtrsim 10^{22}$ cm^{-2}. This maximizes the emission brightness of the lines. The optical thickness also ensures that the line emission is nearly independent of N_{H_2}, as well as reducing contamination from background stars, making the analysis more robust;

3. The cloud has a large extent on the sky to ensure the entire cloud is covered by the slit, thus maximizing the observed signal;

4. The cloud has good visibility for a large fraction of the night during the observing period.

2.2. MMT spectroscopy

The observations were obtained with the MMIRS instrument on the MMT over several nights between November 2020 and January 2021 using the K3000 grism, with spectral resolution $R \sim 3000$. The G150 and G157 clouds were observed with two different slit positioning, bringing the total number of targets observed to six. The slit placement for each target is shown in Fig. 1, and their properties are listed in Table 1.

The upper panel of Fig. 2 shows a section of the 1D spectrum in the vicinity of the $(1-0)S(0)$ line, $\lambda = 2.22\mu$m (denoted by the yellow strip). The strong features, including the high peak a few pixels redward of the (1-0)S(0) line, are skylines. We fit and subtract a linear function (black line) from the spectrum, and further integrate the spectrum over the instrument resolution $\Delta\lambda = \lambda/R \approx 7.4 \times 10^{-4} \mu$m ≈ 2.5 pixels. This subtracted-integrated spectrum is shown in Fig. 2, 2nd row. The 3rd and 4th rows show the noise and the SNR. At the (1-0)S(0) line wavelength (orange strip), SNR < 3, and we claim a non-detection. We use 3σ (3rd row) noise level at the (1-0)S(0) wavelength to place an upper limit on the (1-0)S(0) line brightness for all of our targets. We have further increased the limits by a factor of two to account for uncertainties in the flux calibration (Table 1). See Appendix A for more details.

3. Constraints on the CR ionization rate and CR spectrum

In this section we convert our limits on the $(1-0)S(0)$ brightness to upper limits on ζ in the target clouds, and on the spectral slope of low-energy CRs, based on both an analytic and a numerical model.

3.1. The CR ionization rate - analytic model

As discussed in B20 CRs (and secondary electrons produced by CRs) penetrate into molecular clouds and excite the rovibrational levels of H_2 leading to line emission in the NIR. Unlike photo excitation at the cloud surface, or excitation by the H_2 formation process, CRs are much more efficient in exciting two specific energy states, the $v = 1$, $J = 0$ and $v = 1$, $J = 2$ levels (see also Gredel & Dalgarno 1995), resulting in efficient emission of the $(1-0)S(0)$, $(1-0)O(2)$, $(1-0)Q(2)$ and $(1-0)O(4)$ lines in the 2-3 μm range (B20).

Since the cloud density is low compared to the levels' critical density, the line emission surface brightness is directly proportional to the CR excitation rate, with

$$I_{ul} = \frac{1}{4\pi} g N_{H_2} \zeta_{ex} p_u \alpha_{(u)l} E_{ul} , \tag{1}$$

(Eq. 1 in B20, see also Appendix B). Here I_{ul} is the line brightness (erg cm^{-2} s^{-1} sr^{-1}), N_{H_2} is the H_2 column density, $g \equiv \frac{1-e^{-0.9N_{22}}}{0.9N_{22}}$ is a factor that accounts for the optical thickness where $N_{22} \equiv N_{H_2}/(10^{22}$ cm$^{-2})$, and ζ_{ex} is the total CR excitation rate, including all H_2 levels. The remaining factors are set by atomic physics: p_u is the fraction of all excitations that go onto the specific level of interest, u, $\alpha_{(u)l}$ is the branching ratio for radiative decay to level l (from upper level u), and E_{ul} is the energy of the transition. The subscripts, u and l denote the "upper" and "lower" states of the transition. In our case, for the $(1-0)S(0)$ line, and for CR excitation we have, $u : (v = 1, J = 2)$, $l : (v = 0, J = 0)$, $p_u = 0.47$, $\alpha_{(u)l} = 0.3$, $E_{ul} = 0.56$ eV (B20, Table 1).

The total H_2 CR excitation rate, ζ_{ex}, and the H_2 ionization rate, ζ, are proportional, with $\varphi \equiv \zeta_{ex}/\zeta \approx 5.8$ (Gredel & Dalgarno 1995). Plugging this back into Eq. (1) and inverting we get:

$$\zeta = 4\pi I_{ul}(\varphi p_u \alpha_{(u)l} E_{ul} g N_{H_2})^{-1}$$
$$= 2.6 \times 10^{-16} \left(\frac{I_{(1-0)S(0)}}{10^{-7} \text{ erg cm}^{-2} \text{ s}^{-1} \text{ sr}^{-1}} \right) \frac{0.66}{g} \frac{1}{N_{22}} \text{ s}^{-1} . \tag{2}$$

In the numerical evaluation we focused on the $(1-0)S(0)$ transition at $N_{22} = 1$ (for which $g = 0.66$).

For G150, $N_{22} = 0.9$, $g = 0.69$, and $I_{S(0)} \leq 8.3 \times 10^{-8}$ erg cm^{-2} s^{-1} sr^{-1} (Table 1). We obtain a 3σ upper limit $\zeta \leq 2.3 \times 10^{-16}$ s^{-1}. We repeat this exercise for the rest of our observed targets and present the results in Table 1.

We note that in the original derivation, ζ does not vary with cloud depth. In practice, as CRs propagate into a cloud they lose energy and ζ decreases. In the presence of CR attenuation, Eqs. (1-2) may still be valid under some circumstances (and after applying a correction factor), in which case ζ represents the attenuated CR ionization rate in the cloud interior. See Appendix B, for more details and limiting cases.

3.2. The CR spectrum - numerical model

We use a detailed numerical model to connect the CR ionization and excitation rate in the cloud interior to the initial spectrum of low-energy CR protons that is impinging the cloud on its boundary. This allows us to convert the upper limit on the $(1-0)S(0)$ line brightness into a constraint on the low-energy interstellar CR proton spectrum. We account for energy losses due to H_2 ionization, dissociation, excitation, and momentum transfer, and calculate the modulation of the CR spectrum (of both primary and secondary CRs) as CRs propagate into a cloud. We derive the resulting H_2 excitation rate and the brightness of the H_2 rovibrational emitted lines for different interstellar CR spectra. For more details, see Padovani et al. (2022, in prep.), hereafter P22.

For the interstellar CR proton spectrum, we consider a continuous set of models that are characterized by their low-energy spectral slope, α. An example of three models is shown in Fig. 3 (left panel). At energies $E \gtrsim 1$ GeV the proton spectrum is constrained by AMS-02 (Aguilar et al. 2015) For $E = 3 - 300$ MeV, the proton spectrum has been observed by the two Voyager spacecrafts (Cummings et al. 2016; Stone et al. 2019). However, it is not clear whether Voyager is probing a representative interstellar CR field. First, the magnetic field direction measured by the Voyager probes did not show the change expected if they were beyond the influence of solar modulation (Gloeckler & Fisk 2015; Padovani et al. 2018). Second, even if the probes are not under the influence of solar modulation, they are still in the local bubble. Consequently, there is a substantial uncertainty about the low-energy proton spectrum at $E \lesssim 1$ GeV, and hence we
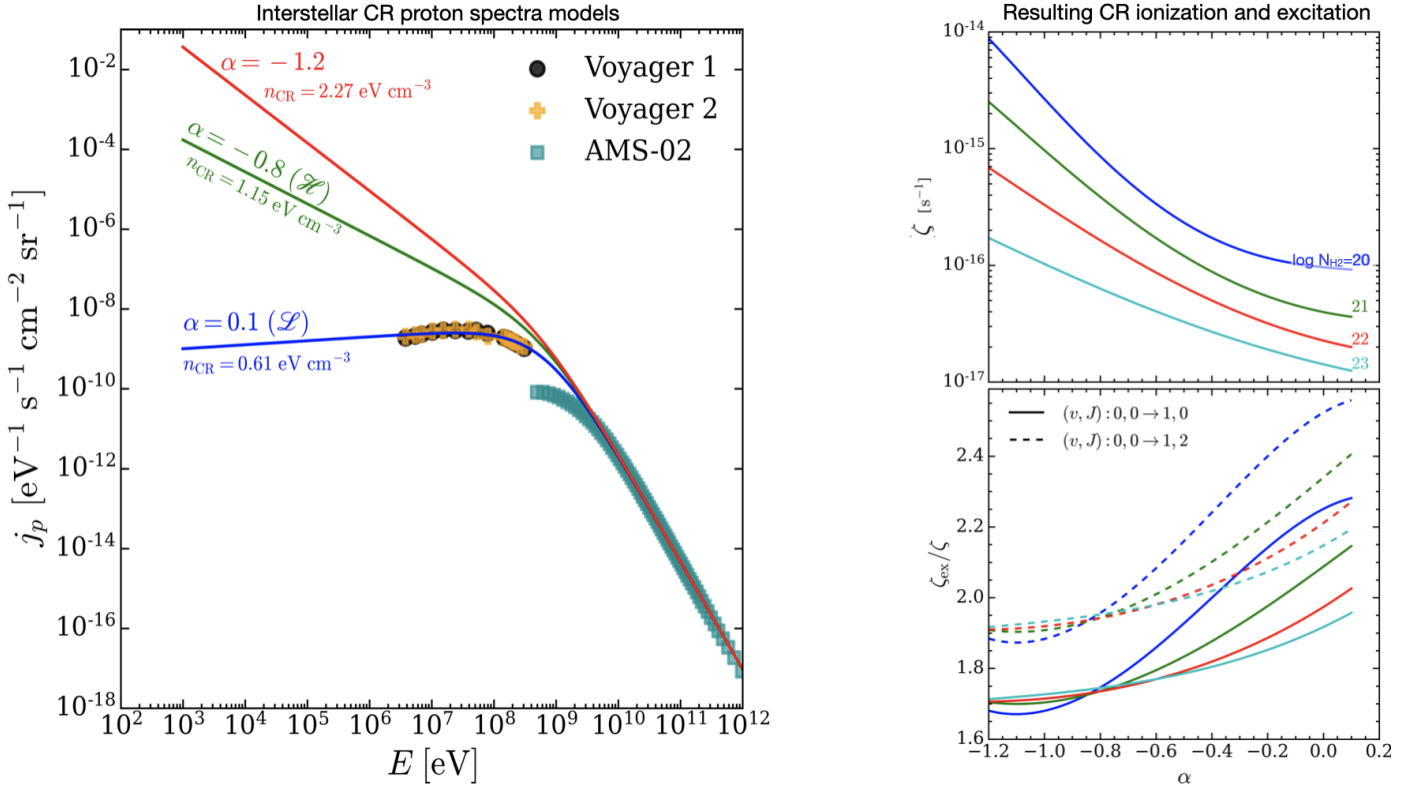
Fig. 3. Left: the spectrum of interstellar CR protons that are impinging on the cloud at its boundary ($N_{H_2} = 0$). For energies $E \gtrsim 1$ GeV, the spectrum is constrained by AMS02 observations (Aguilar et al. 2015). At lower energies, the spectrum is constrain by Voyager observations (Cummings et al. 2016; Stone et al. 2019), however, since these observations are likely not probing a representative interstellar spectrum (see §3.2), we consider different models with different low-energy spectral slopes, α. Right: the resulting CR ionization and excitation rates inside the cloud as a function of α and the clouds' molecular column density N_{H_2}, as calculated by our CR propagation model.
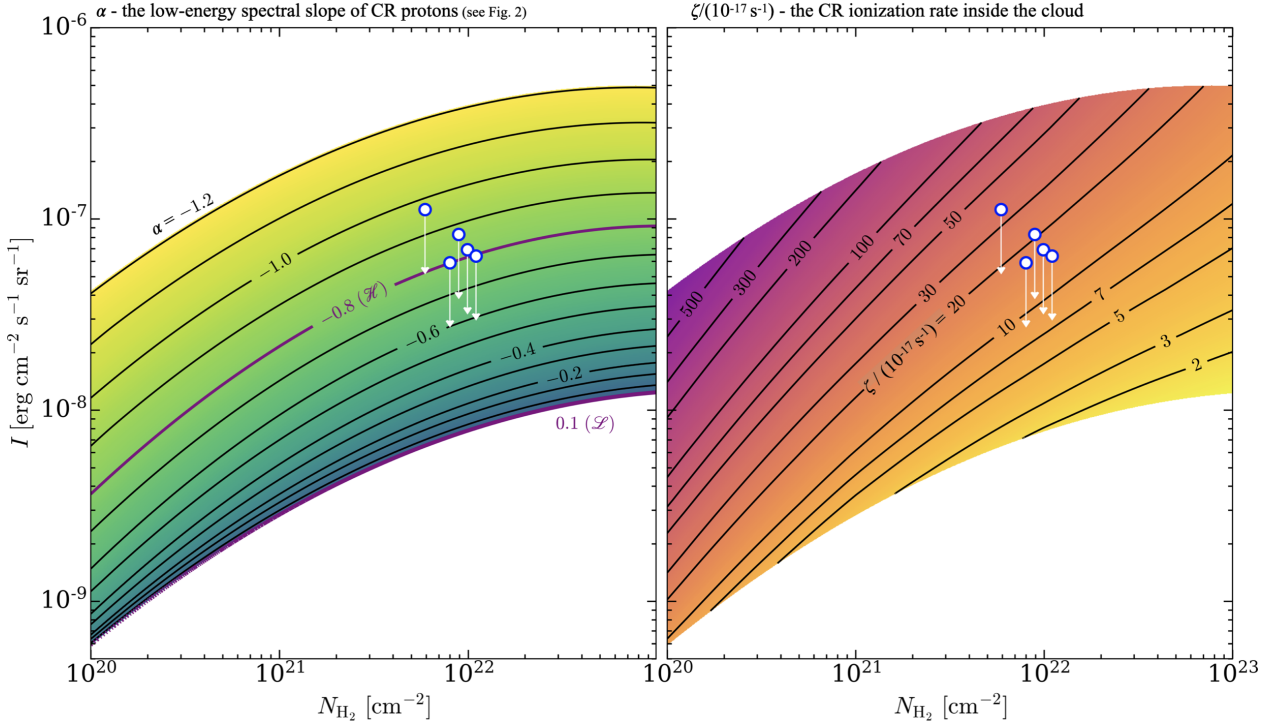

Fig. 4. The $(1-0)S(0)$ line brightness as a function of the cloud H_2 column density for different models of the interstellar CR proton spectrum impinging upon the cloud (see Fig. 3). Contours: the CR spectral slope α (left), and the (attenuated) CR ionization rate inside the cloud (right). The five markers are our 3σ upper limits on the $(1-0)S(0)$ line, which translate into upper limits on ζ and lower limits on α.

Table 1. Observations and Limits on the CR ionization rate and the spectral slope of low-energy CRs

Cloud Name	Coordinates RA-DEC (J2000)	d distance to cloud (pc)	N_{H_2} H$_2$ column density (cm^{-2})	t_{exp} Exposure time (minutes)	$I_{(1-0)S(0)}$ $(1-0)$S(0) surface brightness (erg cm^{-2} s^{-1} sr^{-1})	ζ ionization rate - analytic (s^{-1})	ζ ionization rate - numeric (s^{-1})	α low-energy spectral slope of CR protons
G150	04:25:04.0 +54:56:57.1	170	8.9×10^{21}	211	$\leq 8.3 \times 10^{-8}$	$\leq 2.3 \times 10^{-16}$	$\leq 2.1 \times 10^{-16}$	≥ -0.87
G150 (pos. 2)	04:14:41.8 +55:11:18.3	170	5.9×10^{21}	181	$\leq 1.2 \times 10^{-7}$	$\leq 4.4 \times 10^{-16}$	$\leq 3.6 \times 10^{-16}$	≥ -0.97
G157	04:01:39.8 +41:12:20.0	450	9.9×10^{21}	181	$\leq 6.9 \times 10^{-8}$	$\leq 1.8 \times 10^{-16}$	$\leq 1.7 \times 10^{-16}$	≥ -0.82
G157 (pos. 2)	04:01:38.5 +41:04:03.8	450	8.0×10^{21}	191	$\leq 5.9 \times 10^{-8}$	$\leq 1.8 \times 10^{-16}$	$\leq 1.7 \times 10^{-16}$	≥ -0.80
G163	4:25:22.2 +37:09:51.6	450	1.1×10^{22}	181	$\leq 6.4 \times 10^{-8}$	$\leq 1.5 \times 10^{-16}$	$\leq 1.5 \times 10^{-16}$	≥ -0.79
G198	05:52:18.5 +08:22:45.8	445	6.8×10^{21}	186	-	-	-	-

(1) The cloud names are abbreviations of the full designations used in the GCC survey (Juvela et al. 2012): G150.47+3.93, G157.08-8.69, G163.82-8.44, G198.58-9.10, respectively. (2) The coordinates correspond to the slit center position. (3) Distances adopted from Juvela et al. (2012, Table 1). (4) H$_2$ columns are based on A_K dust extinction measurements using the NICEST method (Lombardi 2009)[2], assuming a standard extinction curve (Draine 2011), and averaged along the slit. (5) Exposure times are the integrated on-source exposures. (6,7,8) The upper limits are based on the 3σ noise level at the (1-0)S(0) line wavelength, after applying an additional factor of two multiplicative factor to account for uncertainties in the flux calibration. (9) The corresponding lower limits on the low energy spectral slope of interstellar CR protons.

consider an array of models with different α values. For the CR electron flux we follow P22 (their Eq. 2 and Table 2).

The total energy density, n_{CR}, for the various models is indicated in Fig. 3 (left). The steeper spectra (smaller α values) have higher CR fluxes, and consequently, ζ increases as α decreases - see Fig. 3, upper-right panel. Fig. 3 also shows that for a given spectrum (fixed α), ζ decreases with increasing cloud column N_{H_2}. This is because the CRs lose energy as they propagate into the cloud and the CR flux at low energies decreases with N_{H_2} (see P22, Fig. 4). The lower-right panel of Fig. 3 shows the excitation to ionization rate ratio for the two states $v = 1$, $J = 0$ and $J = 2$, which dominate the CR excitation of H$_2$ (B20). This ratio varies with N_{H_2} and α, however the variations are rather mild. Summing up the excitation of both levels, we obtain $\phi \equiv \zeta_{ex}/\zeta = 3.6$ to 4.8. Excitation to $v \geq 2$ levels increase ζ_{ex} by ≈ 10 % giving $\phi = 4-5.3$, in reasonable agreement with the value used by B20.

Using our CR propagation model we have generated a lookup plot, Fig. 4, that predicts the interstellar proton CR spectral slope α (i.e., the models shown in Fig. 3), and the CR ionization rate in the cloud interior, $\zeta(N_{H_2})$, given a measurement of the $(1-0)$S(0) line brightness and the cloud's column N_{H_2} (see P22 for additional lines). For a given α value, the integrated line intensity increases with N_{H_2} in the optically thin limit, and then saturates at $N_{H_2} \approx 10^{22}$ cm^{-2} as the cloud becomes optically thick due to dust absorption (see Appendix B). At a given N_{H_2}, ζ increases with decreasing α because the lower α models correspond to higher CR fluxes.

The five markers show our 3σ upper limits on the $(1-0)$S(0) line for G150, G150p2, G157, G157p2 and G163. Correspondingly, the lower limit on α is within -0.87 and -0.67 for these clouds, and the upper limit on ζ is within 1.0 and 2.6×10^{-16} (see Table 1). The ζ values are in excellent agreement with the analytic model (§3.1), and are in agreement with the general range of ζ values in the literature, deduced via absorption spectroscopy of various molecules (see P22 for a comprehensive comparison).

4. Future prospects for JWST

Despite our long integration time the H$_2$ rovibrational lines were not detected in any of our 6 targets. This is because at this wavelength range ($\approx 2 - 3 \ \mu$m) the spectrum is contaminated by thermal emission, absorption, and strong skylines from the atmosphere. We estimate JWST/NIRSpec's expected sensitivity for line detection. First, let us focus on the $(1-0)$O(2) line at $\lambda = 2.63 \ \mu$m. This line is blocked for ground-based observations, but is predicted to be the strongest line for CR excitation (B20). The O(2) line emission from a cloud with column $N_{22} = 1$ illuminated by a CR spectrum with slope $\alpha = 0.1$ (for which $\zeta \approx 10^{-17}$ s^{-1}), is $I \approx 3 \times 10^{-8}$ erg cm^{-2} s^{-1} sr^{-1} (P22). Using JWST's exposure time calculator (ETC) with $t_{exp} = 1.25$ hrs we obtain a SNR = 1.24 per shutter. Integrating over the $365 \times 2 = 730$ shutters along the spatial direction gives SNR ≈ 33.5. Importantly, the line brightness that we assumed corresponds to a proton spectrum with $\alpha = 0.1$ - this is the spectrum with the shallowest slope, the lowest ζ value, and the faintest emission among all models

(see Fig. 4, and Fig. 8 in P22 for additional H_2 lines). Thus, in practice, JWST will be sensitive to the entire range of possible CR models, and will be able to robustly constrain the proton spectrum at low energies.

Another advantage of JWST's high sensitivity is that it will allow the discrimination of various H_2 excitation mechanisms, including excitation by CRs, UV pumping and chemical excitation from H_2 formation. As discussed in B20, these excitation processes exhibit different line ratios. For example, the line ratio $\eta \equiv I_{(1-0)S(1)}/I_{(1-0)S(0)}$: for pure UV excitation $\eta \approx 2$ (Black & van Dishoeck 1987; Sternberg 1988), for pure H_2 formation $\eta \approx 3.5 - 5.6$ (Le Bourlot et al. 1995), whereas for pure CRs $\eta \approx 0.04$ or lower (B20). Thus, measured line ratios may be used to determine the relative importance of each excitation process and the individual values of the CR and the FUV radiation fluxes (see Appendix C for strategies for separating FUV excitation vs CR excitation). To evaluate the ability of JWST to detect the fainter lines, we consider the $(1-0)S(1)$ line ($\lambda = 2.12 \ \mu$m), excited by the mean FUV interstellar radiation field (Draine 1978; Bialy 2020b), for which $I = 1.8 \times 10^{-8}$ erg cm^{-2} s^{-1} sr^{-1} (Eqs. 8-9, B20; this analytic value is in good agreement with the numerical results discussed in Appendix C). Using JWST/NIRSpec's ETC with $t_{\mathrm{exp}} = 1.25$ hrs we obtain a SNR = 1.22 per shutter and an integrated SNR ≈ 33 (over all shutters). Similarly, other H_2 rovibrational lines may be also robustly detected.

Given a detection, we may also restrict the shutter integration over a smaller number of shutters. This will sacrifice the SNR but will allow to derive the CR ionization rate in different positions along the observed cloud, allowing to obtain, for the first time, the ζ gradient across a starless core with a very high spatial resolution of[3] $\sim 10^{-3}$ pc.

X-rays have a similar effect on H_2 excitation as CRs. This is because in both case, the H_2 is excited mainly by the secondary electrons (see P22 for a comparison of primary vs secondary excitation). Thus, when constraining CR properties, it is important to ensure that the observed cloud is starless. On the other hand, H_2 emission lines may be used to constrain the properties of the X-ray irradiation, if the targeted clouds are specifically chosen to be in the vicinity of known X-ray sources, e.g., near X-ray binaries or active galactic nuclei.

5. Conclusions

Utilizing the "direct method" H_2 analysis (including the B20's analytic model and P22's numerical model) and deep NIR spectroscopy of several dense clouds, we placed upper limits on the ionization rate and on the spectral slope of low-energy CR protons, ruling out steep CR spectral models. While ground based observations cannot detect the H_2 rovibrational lines, JWST/NIRSpec will be able to efficiently detect them, and thus to determine the relative roles of CR versus UV excitation, and to constrain the otherwise elusive low-energy CR spectrum. Extending this observation to a sample of clouds located in different proximity to potential CR sources, as well as in different positions within a molecular cloud, will allow to constrain fluctuations in the CR ionization rate, the source of low-energy CRs and the CR propagation process.

References

Aguilar, M., Aisa, D., Alpat, B., et al. 2015, Phys. Rev. Lett., 114, 1
Baines, D., Giordano, F., Racero, E., et al. 2017, Publ. Astron. Soc. Pacific, 129, 1
Bialy, S. 2020a, Nat. Commun. Phys., 3, 32
Bialy, S. 2020b, ApJ, 903, 62
Bialy, S., Bihr, S., Beuther, H., Henning, T., & Sternberg, A. 2017, ApJ, 835, 126
Bialy, S., Neufeld, D., Wolfire, M., Sternberg, A., & Burkhart, B. 2019, ApJ, 885, 109
Black, J. H. & van Dishoeck, E. F. 1987, ApJ, 322, 412
Bron, E., Le Bourlot, J., & Le Petit, F. 2014, A&A, 569, A100
Caselli, P., Ceccarelli, C., Caselli, P., & Ceccarelli, C. 2012, A&ARv, 20, 56
Chilingarian, I., Beletsky, Y., Moran, S., et al. 2015, Publ. Astron. Soc. Pacific, 127, 406
Cummings, A. C., Stone, E. C., Heikkila, B. C., et al. 2016, ApJ, 831, 18
Dalgarno, A. 2006, Proc. Natl. Acad. Sci. United States Am., 103, 12269
Draine, B. T. 1978, ApJS, 36, 595
Draine, B. T. 2003, ApJ, 598, 1017
Draine, B. T. 2011, Physics of the interstellar and intergalactic medium
Favre, C., Ceccarelli, C., López-Sepulcre, A., et al. 2018, ApJ, 859, 136
Fontani, F., Ceccarelli, C., Favre, C., et al. 2017, A&A, 605, A57
Gaches, B. A. L., Offner, S. S. R., & Bisbas, T. G. 2019, ApJ, 878, 105
Girichidis, P., Offner, S. S., Kritsuk, A. G., et al. 2020, Sp. Sci. Rev., 216, 68
Glassgold, A. E., Galli, D., & Padovani, M. 2012, ApJ, 756, 157
Gloeckler, G. & Fisk, L. A. 2015, ApJL, 806, L27
González-Alfonso, E., Fischer, J., Bruderer, S., et al. 2018, ApJ, 857, 66
Gredel, R. & Dalgarno, A. 1995, ApJ, 852
Guelin, M., Langer, W., & Wilson, R. 1982, A&A, 107, 107
Indriolo, N. & Mc Call, B. J. 2013, Chem. Soc. Rev., 42, 7763
Indriolo, N. & McCall, B. J. 2012, ApJ, 745, 91
Jo, Y.-S., Seon, K.-I., Min, K.-W., Edelstein, J., & Han, W. 2017, ApJS, 231, 21
Juvela, M., Ristorcelli, I., Pagani, L., et al. 2012, A&A, 541, A12
Kelson, D. 2003, Publ. Astron. Soc. Pacific, 115, 688
Le Bourlot, J., des Forêts, G. P., Roueff, E., Dalgarno, A., & Gredel, R. 1995, ApJ, 449, 178
Le Petit, F., Nehme, C., Le Bourlot, J., & Roueff, E. 2006, ApJS, 164, 506
Le Petit, F., Ruaud, M., Bron, E., et al. 2016, A&A, 585, A105
Lee, D.-H., Yuk, I.-S., Jin, H., et al. 2006, ApJ, 644, L181
Lombardi, M. 2009, A&A, 493, 735
Luhman, M. L. & Jaffe, D. T. 1996, ApJ, 463, 191
Luhman, M. L., Jaffe, D. T., Keller, L. D., & Pak, S. 1994, ApJ, 436, L185
Mattila, K., Haas, M., Haikala, L. K., et al. 2018, A&A, 617, A42
Müller, H. S., Muller, S., Schilke, P., et al. 2015, A&A, 582, 2
Neufeld, D. A. & Spaans, M. 1996, ApJ, 473, 894
Neufeld, D. A. & Wolfire, M. G. 2017, ApJ, 845, 163
Padovani, M., Galli, D., & Glassgold, A. E. 2009, A&A, 501, 619
Padovani, M., Galli, D., Hennebelle, P., Commerçon, B., & Joos, M. 2014, A&A, 571, 1
Padovani, M., Ivlev, A. V., Galli, D., & Caselli, P. 2018, A&A, 614, A111
Padovani, M., Ivlev, A. V., Galli, D., et al. 2020, Sp. Sci. Rev., 216, 29
Skrutskie, M. F., Cutri, R. M., Stiening, R., et al. 2006, AJ, 131, 1163
Sternberg, A. 1988, ApJ, 332, 400
Sternberg, A. & Dalgarno, A. 1989, ApJ, 338, 197
Stone, E. C., Cummings, A. C., Heikkila, B. C., & Lal, N. 2019, Nat. Astron., 3, 1013
van der Tak, F. F. S. & van Dishoeck, E. F. 2000, A&A, 358L, 79V
Zhao, B., Tomida, K., Hennebelle, P., et al. 2020, Sp. Sci. Rev., 216, 43

---

[3] We used NIRSpec's shutter angular size 0.53″ at a distance $d = 500$ pc

Appendix A: Data reduction and noise derivation

The observations were obtained with the MMIRS instrument on the MMT over several nights between November 2020 and January 2021, using the K3000 grism with a 0.4 arcsec slit width, yielding a spectral resolution $R \sim 3000$. (using a wider slit would increase the amount of light reaching the instrument, but would also broaden the sky emission lines). The MMIRS slit is 7 arcmin long, which is a good match to the angular size of the targets. The slit was generally placed on the peak of the column density distribution. To improve sky subtraction we alternated object frames to sky frames, which were obtained by moving the telescope by 30 arcmin along the direction of the slit. Each target was observed in 5-minute frames for a total of approximately 180 min on source and 180 min on sky.

A.1. Data reduction

The observations were reduced with the MMIRS data reduction pipeline (Chilingarian et al. 2015). Since the emission from the cloud covers the entire extent of the longslit, it is not possible to model and subtract the sky emission from the data, and we skipped the sky subtraction step that uses the Kelson (2003) method. Instead, we rely only on the difference of source-sky frames to suppress the sky emission.

After masking bad pixels and stellar traces, which usually account for 20-30% of the pixels in the 2D reduced spectra, we stack the spectrum of each target along the slit and obtain the 1D spectrum. We apply a theoretical flux calibration based on the telescope collecting area, angular size of the observed region, exposure time, expected efficiency of the instrument, and we convert the spectrum from counts to flux density per unit solid angle (erg cm^{-2} s^{-1} μm^{-1} sr^{-1}). We compare this flux calibration to that obtained using observations of standard stars, and we conclude that the overall flux calibration is reliable within a factor of two.

A.2. Deriving the noise and placing upper limits on line brightness

Our observations span the wavelength range $1.890 - 2.509$ μm, which contains several H$_2$ transitions. However, most of these are either expected to be too weak to be detected, or strongly affected by sky emission and absorption. This leaves two lines of interest: $(1-0)S(0)$ and $(1-0)S(1)$; we focus on the former since for CR excitation in cold molecular clouds, (1-0)S(0) is expected to strongly dominate over (1-0)S(1) (see B20, Table 1). We still checked for $(1-0)S(1)$ but did not detect any emission.

The upper panels of Fig. 2 and Fig. A.1 show a section of the 1D spectrum in the vicinity of the $(1-0)S(0)$ line ($\lambda = 2.22\mu$m, denoted by the yellow strip) for all of our targets. The strong features, including the high peak a few pixels redward of the (1-0)S(0) line, are skylines which we use to explicitly verify that the wavelength calibration is very precise. We identify a region around the (1-0)S(0) line that is devoid of skylines, marked as the blue strip, hereafter the "good λ range". For this wavelength range we fit a linear function, shown as the black line, and subtract it from the spectra. Since the H$_2$ emission lines are very narrow (the instrument resolution is ≈ 100 km/s. In contrast, thermal broadening and turbulent broadening for typical cold clouds are ≈ 0.2 km/s and ≈ 2 km/s), the line, if observed, would be broadened to the instrument's spectral resolution, $\Delta\lambda = \lambda/R \approx 7.4 \times 10^{-4}$ μm ≈ 2.5 pixels. We have also verified this value by measuring the width of nearby skylines in the

observed spectrum. Thus, to search for a line emission, we integrate the subtracted spectrum over $\Delta\lambda$. We denote this subtracted and integrated spectrum $I_{\rm sub,int}$, and show it in the 2$^{\rm nd}$ rows of Figs. 2, A.1. The $(1-0)S(0)$ emission line is not detected for any of the targets.

To place an upper limit on the (1-0)S(0) line brightness we evaluate the noise:

1. In the 2D spectra, we sum in quadrature the error on each pixel, along the spatial dimension (excluding the masked pixels). The error per pixel is provided by MMIRS's pipeline, based on the standard deviation (STD) in the pixel flux across individual time frames. We also compared it with the signal's STD across the spatial and wavelength directions, and also with a theoretical error estimate based on calculations of the Poisson noise and readout noise and found a good agreement. We integrate these errors over $\Delta\lambda$ and denote the result $\sigma_{\rm pipe}$.

2. Comparing $\sigma_{\rm pipe}$ with the fluctuations of $I_{\rm sub,int}$ along the wavelength direction, we find that the $\sigma_{\rm pipe}$ values are too optimistic. For example, the calculated STD of $I_{\rm sub,int}$ within the "good λ range" (the blue strip in Fig. 2) for G150 is 1.6×10^{-8} erg cm^{-2} s^{-1} sr^{-1}, a factor of 2.1 higher than $\langle\sigma_{\rm pipe}\rangle$ (average over the good λ range). Thus, for G150, we correct the $\sigma_{\rm pipe}$ values by multiplying them by 2.1. For the rest of our targets, the correction factors range within 1.5 to 2.7. This correction ensures that the STD of $I_{\rm sub,int}$ equals the mean σ values, as it should. We denote the corrected errors σ.

The corrected errors, σ, are shown in the 3$^{\rm rd}$ rows of Figs. 2, A.1. The 4$^{\rm th}$ rows show the SNR. At the (1-0)S(0) line wavelength (orange strip), SNR < 3, and thus we claim a non-detection. More generally, within the "good λ range", there are fluctuations but overall $\|{\rm SNR}\| < 3$, giving confidence in our evaluation of the spectrum and error corrections.

We use the 3σ noise level at the (1-0)S(0) line wavelength to place an upper limit on the (1-0)S(0) line brightness. We further multiply the 3σ values by a factor of 2 to account for the flux calibration uncertainty (see above). This gives us robust upper limits on the (1-0)S(0) line brightness, which we report in Table 1, and show in Fig. 4.

Appendix B: Analytic model for the case of cosmic ray attenuation

In this appendix we discuss a generalization for Eq. (1) for the case of a non-constant ζ, i.e., a case where CR energy losses are taken into account and thus result in a ζ that decreases with cloud depth. This case was also discussed in B20 (see their Methods section). However, as we discuss below, B20's conclusion that for a varying CR rate, Eq. (1) still holds if $\zeta N_{\rm H_2}$ is replaced with $\int \zeta \, {\rm d}N_{\rm H_2}$ is only correct in the case of optically thin gas ($\tau \ll 1$). As we show for a varying ζ and an optically thick gas, an analytic solution can still be obtained, but it is more involved.

The contribution to the line emission from an infinitesimal slab, ${\rm d}N_{\rm H_2}$, that is excited by CR particles and their produced secondary electrons, may be written as:

$${\rm d}I_{ul} = \frac{1}{4\pi} {\rm d}N_{\rm H_2} \zeta_{\rm ex}(N_{\rm H_2}) p_u \alpha_{(u)l} {\rm e}^{-\tau} \tag{B.1}$$

where $N_{\rm H_2}$ is the integrated column from cloud edge to the position of the infinitesimal slab, $\tau = \sigma_{d,\rm H_2} N_{\rm H_2}$ is the optical depth
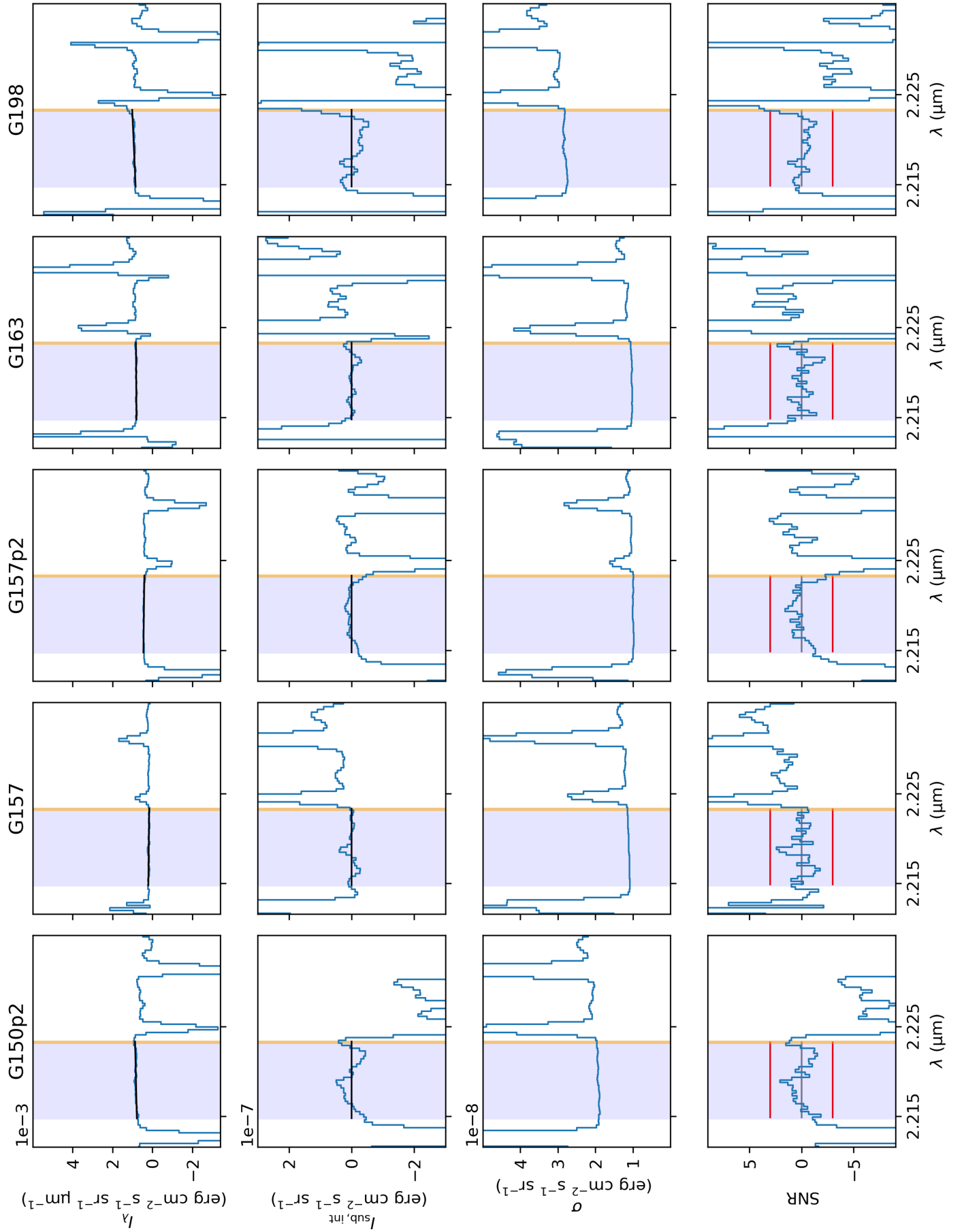
Fig. A.1. Same as Fig. 2, but for the rest of our targets.

and and $\sigma_{d,H_2} \approx 0.9 \times 10^{-22}$ cm^2 is the dust absorption cross section per H_2 molecule, at the wavelength of interest (Draine 2003, B20). Dust absorption dominates the opacity for the considered lines. The meaning of the rest of the symbols is as described in §3.1.

For a cloud of total H_2 column density N_{H_2}, we integrate Eq. (B.1) and obtain the emitted line brightness:

$$I_{ul} = \int dI_{ul} = \frac{1}{4\pi} p_u \alpha_{(u)l} \int_0^{N_{H_2}} \zeta_{ex}(N'_{H_2}) e^{-\tau} dN'_{H_2} . \tag{B.2}$$

This integral may be solved under some simplifying assumptions.

B.1. Constant CR excitation rate: both optically thin and thick regimes

For a constant CR excitation rate (i.e., where ζ_{ex} is not a function of N_{H_2}) we can pull ζ_{ex} out of the integral and we get

$$I_{ul} = \frac{1}{4\pi} p_u \alpha_{(u)l} \zeta_{ex} \int_0^{N_{H_2}} e^{-\tau} dN'_{H_2}$$
$$= \frac{1}{4\pi} p_u \alpha_{(u)l} \zeta_{ex} g N_{H_2} \tag{B.3}$$

where

$$g \equiv \frac{1 - e^{-\tau}}{\tau} = \frac{1 - e^{-0.9N_{22}}}{0.9N_{22}} , \tag{B.4}$$

and $N_{22} \equiv N_{H_2}/(10^{22}$ cm$^{-2})$. This converges with Eq. (1). The g factor includes the optical thickness effect. For small column densities ($\tau \ll 1$), $g \to 1$ and $I_{ul} \propto N_{H_2}$ as expected for optically thin emission. As N_{H_2} increases, I_{ul} increases until at sufficiently large columns ($\tau \gtrsim 1$), $g \to \tau^{-1} = (0.9N_{22})^{-1}$. In this limit I_{ul} saturates and becomes independent of N_{H_2}. This is the optically thick regime.

B.2. Non constant CR excitation rate: the optically thin regime

In practice, the CR excitation and ionization rates are expected to vary with cloud depth, due to CR energy losses (Padovani et al. 2009). For a non constant CR excitation rate, but assuming the optically thin regime $\tau < 1$, we have

$$I_{ul} = \frac{1}{4\pi} p_u \alpha_{(u)l} \int_0^{N_{H_2}} \zeta_{ex}(N'_{H_2}) dN'_{H_2} . \tag{B.5}$$

While generally the functional form of $\zeta_{ex}(N_{H_2})$ may be complex, if we are interested in sufficiently small column densities, $N_{H_2} \lesssim 10^{24}$ cm^{-2}, $\zeta_{ex}(N_{H_2})$ may be approximated as a power-law $\zeta_{ex} = \zeta_0 (N_{H_2}/N_0)^{-a}$ where a is typically within the range $(0,1)$, and its exact value depends on the interstellar CR proton spectrum (see Fig. 5 in P22). We get

$$I_{ul} = \frac{1}{4\pi} p_u \alpha_{(u)l} \frac{\zeta_0 N_0}{1-a} \left(\frac{N_{H_2}}{N_0}\right)^{1-a} = \frac{1}{4\pi} p_u \alpha_{(u)l} \zeta_{ex}(N_{H_2}) N_{H_2} \frac{1}{1-a} . \tag{B.6}$$

where $\zeta_{ex}(N_{H_2})$ is the CR excitation rate inside the cloud interior. We see that in the optically thin limit, and for a non-constant CR excitation rate, we still obtain an equation similar to Eq. (1) (with $g = 1$ by definition as we assumed the optically

thin regime), but with a correction factor $1/(1-a)$, which is typically of order unity. The powerlaw a depends on the interstellar CR proton spectrum. For example, for the column density range $N_{H_2} = 10^{20} - 10^{23}$ cm^{-2}, $a \approx 0.38$ for the $\mathcal{H}$ proton spectrum, and $a \approx 0.06$ for the $\mathcal{L}$ proton spectrum (see P22, Fig. 4). For these a values, the correction factor is 1.6 and 1.1, respectively.

B.3. Non constant CR excitation rate: the general case

For the general case where the CR rate varies with cloud depth, and the cloud is not optically thin, the integral may still be solved if we assume a power-law form for $\zeta_{ex}(N_{H_2})$. We get

$$I_{ul} = \frac{1}{4\pi} p_u \alpha_{(u)l} \int_0^{N_{H_2}} \zeta_{ex}(N'_{H_2}) e^{-\tau} dN'_{H_2}$$
$$= \frac{1}{4\pi} p_u \alpha_{(u)l} \zeta_0 \frac{\tau_0^a}{\sigma_{d,H_2}} \int_0^\tau x^{-a} e^{-x} dx$$
$$= \frac{1}{4\pi} p_u \alpha_{(u)l} \zeta_0 \frac{\tau_0^a}{\sigma_{d,H_2}} \gamma(1-a, \tau) \tag{B.7}$$

where we defined $\tau_0 \equiv \sigma_{d,H_2} N_0$, and where γ is the lower incomplete gamma function. In the optically thin limit ($\tau \ll 1$), the gamma function $\gamma(1-a, \tau) \to \tau^{1-a}/(1-a)$ and Eq. (B.7) then approaches the solution in Eq. (B.6) as it should.

Appendix C: H_2 photo-excitation versus cosmic-ray excitation

C.1. FUV and CR excitation - physical processes

Although most of the cloud volume is devoid of FUV radiation due to efficient dust absorption, the ambient interstellar FUV radiation field will lead to H_2 excitation in a thin layer at the cloud envelope, i.e., the photo-dominated region (PDR). Here, FUV photons within the Lyman-Werner band ($11.2 - 13.6$ eV) populate the excited electronic states of H_2, which then radiatively decay, populating the excited rovibrational states of the ground electronic state. These rovibrational states (denoted vJ), radiatively decay producing a rich spectrum of emission lines in the NIR. This FUV excitation produces lines with intensities that may be comparable to those produced by CR excitation. Whether the line emission is dominated by FUV excitation or CR excitation depends on the relative intensity of the FUV radiation field to the CR ionization rate, I_{UV}/ζ, and on the specific line considered (see Eqs.(10-11) in B20), where $I_{UV} = F_{UV}/F_{UV,0}$ is the FUV interstellar radiation flux normalized to the solar neighborhood value $F_{UV,0} = 2.7 \times 10^{-3}$ erg cm^{-2} s^{-1} (Draine 1978; Bialy 2020b)

Interestingly, FUV excitation and CR excitation produce different excitation pattern of the $H_2(vJ)$ levels, and thus predict different ratios for the various H_2 emission lines. This is due to two reasons. First is because the excitation processes are physically different. For FUV excitation, the $H_2(vJ)$ are populated through radiative cascade from the excited electronic states (see above), whereas in the case of CRs, direct impact excitation is important. In this latter process, the secondary electrons produced by CR ionization interact directly with the H_2 nuclei efficiently exciting its first vibrational states (Gredel & Dalgarno 1995, P22). This results in very high ratios for lines emitted from $H_2(v = 1)$. For example, the emission of (1-0)S(0) is strongly enhanced, compared to lines from higher vibrational levels, e.g., (2-1)S(0). This is different from FUV excitation which efficiently excites a large array of levels, including those with high v numbers.
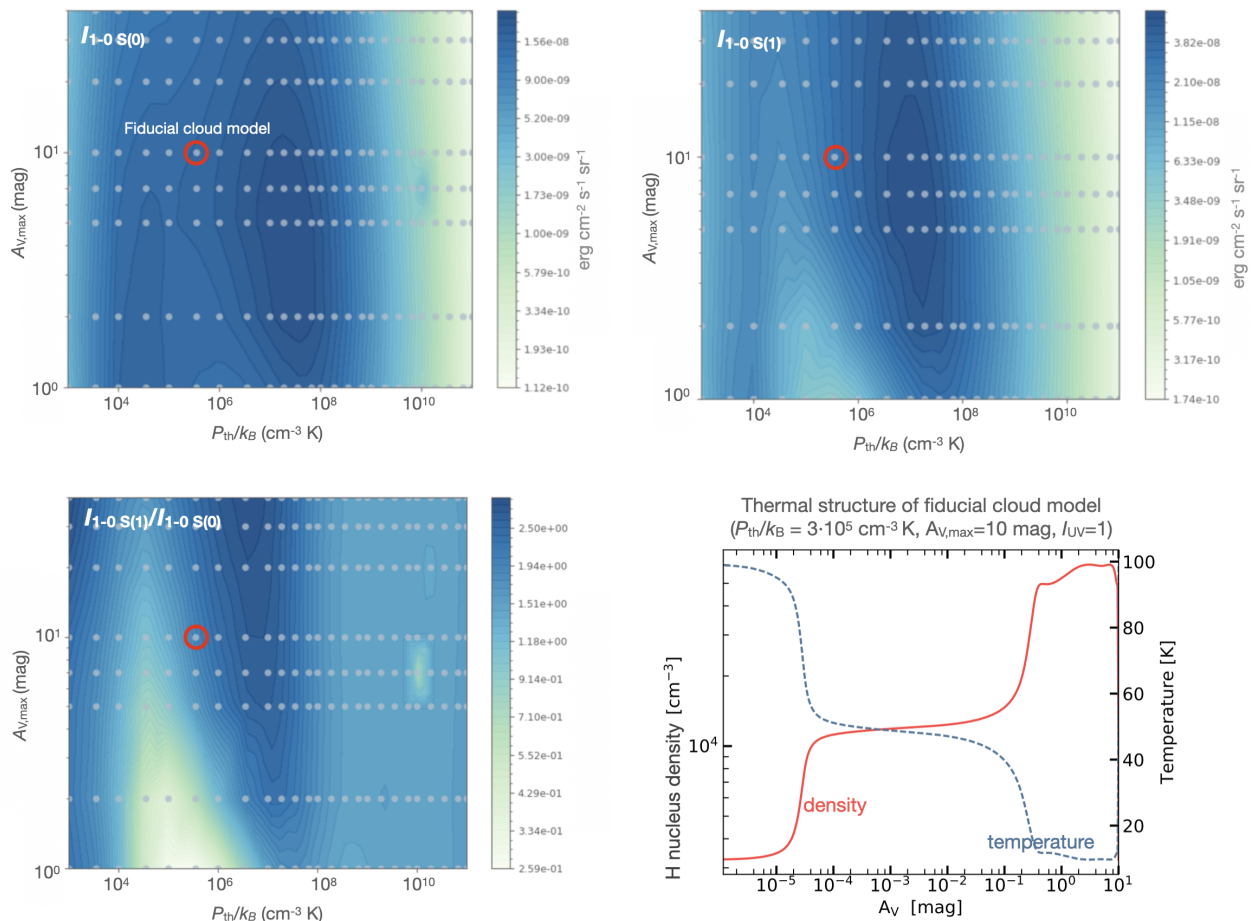
Fig. C.1. The (1-0)S(1) and (1-0)S(0) emission brightness (top), and their ratio (bottom-left) for pure FUV photo-excitation as computed by the isobaric MEUDON PDR models (Le Petit et al. 2006). The line brightness are presented in the parameter space of the cloud's total visual extinction, $A_{V,max}$, versus the cloud's thermal pressure, P_{th}. The points are the locations where the PDR models were computed. The red circle is the fiducial model which represents a typical cloud for our observations, for which we also show the thermal structure of the cloud (bottom-right).

The second reason for the different line ratios for FUV versus CRs, is that the H_2 excitation takes place in different regions of the cloud for the two processes, with significant differences in the gas temperature. The FUV excitation occurs at the cloud outer PDR layer. Here the gas is efficiently heated by the FUV radiation (including: photoelectric heating, H_2 FUV-pumping heating, and H_2 formation heating). The balance between heating and cooling results in gas temperatures of order 100 K. With increasing cloud depth, the FUV radiation is absorbed by dust, and the heating rate decreases. In the deep cloud interiors the H_2 gas is colder and denser, with typical temperatures of order 10 K. These temperature differences result in different ortho-to-para H_2 ratios, such that the ortho-to-para ratio in the cloud interior is significantly lower compared to the PDR. Thus, the FUV excitation results in the emission of both odd and even lines, with comparable intensities, e.g., the (1-0)S(1) and (1-0)S(0), whereas for CR excitation only the H_2 even J states are predominantly excited. For example, for CR excitation, the ratio $\eta \equiv I_{(1-0)S(1)}/I_{(1-0)S(0)}$ is predicted to be very low: for $T = 30$ K, $\eta = 0.04$, and it further decreases with decreasing temperature (B20), whereas for FUV excitation in the warmer PDR, η is typically of order unity (Black & van Dishoeck 1987; Sternberg 1988; Sternberg & Dalgarno 1989).

One may claim that the line ratio is thus not tracing the excitation mechanism (CR vs FUV) but simply the gas temperature. However, in practice, the gas thermal structure is not arbitrary,

but is *controlled* by the intensities of FUV and CRs in the cloud. The gas in the cloud envelope (PDR), is warmer because it is efficiently heated by the FUV radiation. These same FUV photons are also those that excite the H_2 in the PDR. In the deep cloud interior, the gas is colder because the FUV radiation is excluded. Here CRs both excite the H_2 and control the gas temperature (i.e., through ionization and chemical heating; Glassgold et al. 2012).

C.2. Strategies for constraining the contributions of FUV and CR excitation

In a realistic observation, the various H_2 lines and their ratios are influenced by both the FUV excitation (in the PDR) and the CR excitation (in the cloud interior). Thus, any considered line ratio would have an intermediate value between the "pure-FUV" expected value and the "pure-CR" value. The value depends on the FUV and CR intensities, I_{UV}, ζ.

As an example, let us estimate the (1-0)S(1) and (1-0)S(0) line emissions produced by the combined effect of FUV and CR excitation, and the resulting ratio of the two lines for typical starless cores like those observed in the present paper. For the contribution of FUV excitation we utilize the MEUDON PDR model results (Le Petit et al. 2006; Le Bourlot et al. 1995; Bron et al. 2014)[4]. For our fiducial model, we assume $I_{UV} = 1$, $\zeta = 10^{-16}$

[4] https://ism.obspm.fr/ismdb.html

s^{-1}, a total cloud visual extinction $A_{V,max} = 10$ mag ($N_{H_2} \approx 10^{22}$ cm^{-2}), and a cloud thermal pressure $P_{th}/k_B = 3 \times 10^5$ cm^{-3} K (corresponding to inner density and temperature $n_{H_2} \approx 3 \times 10^4$ cm^{-3}, $T \approx 10$ K). We focus on isobaric models as they obey force equilibrium across the cloud layers (i.e., the pressure is constant as a function of cloud depth). In Fig. C.1 we present contour plots showing the line emission of (1-0)S(1), (1-0)S(0), and their ratio, as obtained by the MEUDON PDR model (in which the H$_2$ is excited only by FUV) in the $A_{V,max} - P_{th}$ parameter space. The fiducial model is highlighted by the red circles. The thermal and density structure for the fiducial model is presented in the lower-right panel.

For the fiducial model, pure FUV excitation results in $I^{FUV}_{(1-0)S(0)} = 1.6 \times 10^{-8}$ erg cm^{-2} s^{-1} sr^{-1} and $I^{FUV}_{(1-0)S(1)} = 2.4 \times 10^{-8}$ erg cm^{-2} s^{-1} sr^{-1}, and their ratio is $\eta^{FUV} = 1.5$. For most of the parameter space, these values are only weakly dependent on the exact values of $A_{V,max}$ and P_{th}. For the CR contribution we use Eqs. (3-5) in B20 with $f = 0.16$ appropriate for (1-0)S(0) (Table 1 in B20), $N_{H_2} = 9.4 \times 10^{21}$ cm^{-2} (equivalent to $A_{V,max} = 10$ mag), and $\zeta = 10^{-16}$ s^{-1}. We get $I^{CR}_{(1-0)S(0)} = 3.6 \times 10^{-8}$ erg cm^{-2} s^{-1} sr^{-1}. For (1-0)S(1), CR excitation is negligible compared to FUV excitation. Accounting for both contributions, we get the (1-0)S(0) and (1-0)S(1) line intensities ($I_{(1-0)S(0)}, I_{(1-0)S(1)}$) = $(5.2, 2.4) \times 10^{-8}$ erg cm^{-2} s^{-1} sr^{-1}, and the ratio is $\eta = 0.46$. Thus, if both the (1-0)S(0) and (1-0)S(1) lines are detected, a low η value may be used as an indication of CR excitation in the cloud interior.

While ground-based slit-spectroscopy is not sufficiently sensitive to detect these lines (in clouds exposed to the mean FUV interstellar field, $I_{UV} \approx 1$, where CR excitation is relatively important), an alternative observational strategy is to use a large-beam scanning Fabry-Perot filter. This approach has the advantage that (a) the observing field of view is much larger, and thus the signal is gathered from a large fraction of the cloud area (Luhman et al. 1994; Luhman & Jaffe 1996; see also the discussion in B20, "detectability" section). Indeed, adopting this approach, Luhman et al. (1994) and Luhman & Jaffe (1996) were able to detect very faint and extended emission of the (6-4)Q(1), (1-0)S(1), and (2-1)S(1) lines in various galactic PDRs.

A more robust determination of FUV and CR excitation may be achieved by relying on a large number of H$_2$ transitions, including various ortho-H$_2$ and para-H$_2$ lines, and various vibrational states, $v = 0, 1, 2$, etc. This approach has the advantage that it includes thee two CR excitation effects discussed above (i.e., (1) direct impact versus radiative cascade for CR vs FUV, and (2) different ratios due to the different temperatures in the PDR and inner cloud zone), plus, the fact that the analysis uses many independent lines, makes it less sensitive to observational errors and model uncertainties. Given an observed H$_2$ spectrum, fitting it with a thermo-chemical model that self-consistently calculates the thermal structure and the FUV and CR excitations (including both the exterior PDR zone and the inner CR-dominated region) will allow to reveal the contribution of CRs to the H$_2$ excitation, to robustly determine the values of I_{UV} and ζ, and in turn to constrain the low-energy spectral slope of interstellar CR protons. As we demonstrated in this paper, for clouds illuminated by the typical interstellar radiation field, $I_{UV} \approx 1$, this goal is not achievable from the ground, however, it is very feasible with future space observations, with upcoming JWST (§4). In addition to the high SNR and the detection of many lines simultaneously, another advantage of observations from space is that some lines are completely blocked by the atmosphere and can only be de-

tected from space. Most notably is the (1-0)O(2) line which for CR excitation is predicted to be the brightest H$_2$ line (see Table 1 in B20).

Complementing the NIR spectra with observations at shorter wavelengths may be very useful for constraining I_{UV}. For example, as discussed by Neufeld & Spaans (1996) H$_2$ lines in the red-visible are more readily absorbed by dust and thus preferentially trace the conditions in the cloud outer boundary layer (where FUV excitation dominates). Observations in the FUV, both of the H$_2$ FUV fluorescent lines as well as of the scattered continuum starlight, are useful for constraining the illuminating FUV radiation, as well as of other proprieties of the gas and dust in the PDR (e.g. Lee et al. 2006; Jo et al. 2017; Mattila et al. 2018, see also the discussion in §4.2 in Bialy et al. 2017).